Accelerated multi-property discovery of promising Fe-Si-Al magnetic alloys

Zviad Tsakadze [a,d,1], Li Ping Tan [a,1], Karl
P. Davidson [a], Stéphane Gorsse [b], V. Chaudhary [c], R.V. Ramanujan [a]

a

School of Materials Science and Engineering, Nanyang Technological University, 639798, Singapore

b

CNRS, Université de Bordeaux, Bordeaux INP, ICMCB, UMR 5026, 33600 Pessac, France

c

Industrial and Materials Science, Chalmers University of Technology, SE-41296, Gothenburg, Sweden

d

Residues and Resource Reclamation Centre (R3C), Nanyang Environment and Water Research Institute, Nanyang Technological University, 637141, Singapore

Abstract

Fe-Si binary alloys are one of the most widely used magnetic materials, while some ternary Fe-Si-Al alloys also have excellent magnetic properties and high electrical resistivity. However, none of these alloy compositions meet the multiple superior properties needed in next generation electrical motors. Hence, there is an urgent need to identify novel Fe-Si-Al alloy compositions with a good property set. Compositionally graded materials libraries of Fe-xSi-yAl (x = 3, 7, 9; 0 ≤ y ≤ 8, in wt%) were prepared by mechanical alloying and high throughput spark plasma sintering. The structural, magnetic, mechanical, and electrical properties were rapidly assessed and found to vary significantly with composition. Four promising compositions were down selected based on rapid characterization and property evaluation of the materials libraries. Validation studies of these compositions revealed that the Fe-7Si-8Al composition exhibited an attractive combination of properties. Thus, an accelerated methodology was used to discover new attractive alloy compositions for rotating electrical machines.

Graphical abstract

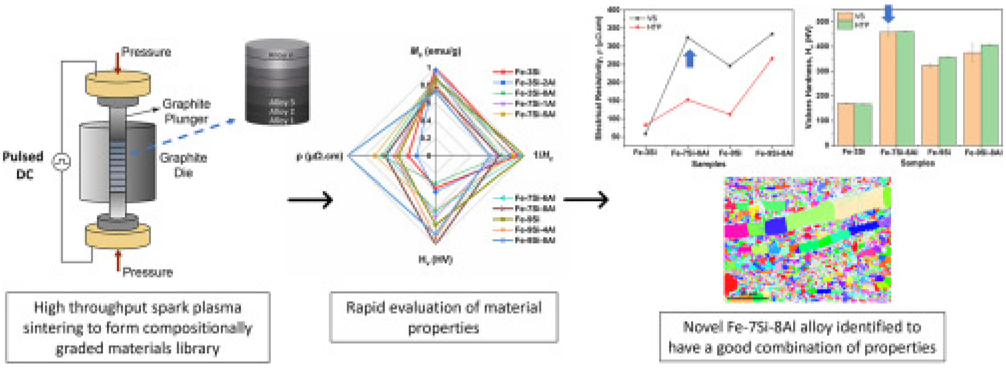

1. Download: Download high-res image (358KB)
2. Download: Download full-size image

- Previous article in issue
- Next article in issue

Keywords

High-throughput methodologies

Materials libraries

Fe-Si-Al alloys

Spark plasma sintering

Mechanical alloying

1. Introduction

Magnetic materials are essential elements of electromagnetic energy conversion technologies. They are widely used in a plethora of electrical and electronic distribution, conversion, and generation devices. These devices include electrical rotating machines, motors, transformers, converters, recording heads, modulators, actuators, sensors etc. [1,2]. However, the present set of magnetic materials are inadequate to meet the next generation of many of these devices. For example, there is an urgent demand for novel large torque, high frequency rotating electrical machines, e.g., electric motors. In a 50 horsepower motor, ~60 % of the energy losses are related to iron loss in the soft magnetic materials used in the motor [3].

Such devices and systems consume a significant fraction of the world's electricity, hence there is high interest in improving their efficiency. Such increased efficiency can be achieved in rotating electrical machine applications by operation at higher frequencies, which can improve power densities [3]. However, the higher frequency leads to greater electrical loss of the rotor, and the magnitude of this loss depends on its electrical resistivity. In motors, the maximum diameter of the rotor can also be limited by the low yield stress of the magnetic material. The required torque also depends on the switching frequency and the number of turns of current carrying wire in the stator [4]. Hence, the mechanical and electrical properties of silicon steels must also be considered, in addition to the earlier focus which was solely on magnetic properties.

Multiple property optimization can also benefit power conversion systems. For example, the permeability was tuned across the diameter of a core material used for power conversion [5]. This can lead to better control of the flux density and the heat distribution, improving the reliability by better tuning of both the thermal and the magnetic properties. Both these examples demonstrate the need for multi-property optimization of magnetic materials.

Fe-Si alloys, also known as electrical steel or silicon steel, have been used for over a century for many soft magnetic applications [6]. Currently, the Fe-3.2Si alloy composition (all compositions in weight%) is the most extensively utilized composition due to advantages such as low cost and a reasonable balance of electrical, magnetic and mechanical properties [3]. Considerable research has been performed to develop alloys with higher Si content since properties such as electrical resistivity can be improved. Fe-6.5Si alloys attracted attention due to their superior electric and magnetic properties, including higher electrical resistivity, higher permeability, low iron loss and near zero magnetostriction [3,[7], [8], [9]]. Compositions with even higher Si content were explored as well [[10], [11], [12]]. Alloys with low Si content exist in a body-centred cubic (BCC) structure, also known as the A2 structure. At temperatures below 500 °C, a Si content of 5.3 % leads to B2 ordering. D03 ordering occurs above 6 % Si [3]. The A2, B2, and D03 structures represent αFe, CsCl-type AB compounds, and $AlFe_3$-type A_mB_n compounds, respectively [3]. The difference between the B2 and D03 phases lies in the ordering of the Si atoms in the crystal structure, with D03 being more ordered than B2 [3].

Alloys with a Si content beyond 6 % are very brittle due to the formation of the ordered B2 and the D03 phases, making such compositions unsuitable for traditional casting and rolling processes [6,9,13]. To fabricate high silicon steels, alternative processing methods such as rapid quenching, magnetron sputtering, physical vapour deposition, spray forming, additive manufacturing, mechanical alloying, and thermo-mechanical processing have been trialed [1,3]. These processing routes can minimize the formation of undesirable ordered phases.

In this work, Al is chosen as the alloying element for Fe-Si. Prior investigations done about a century ago proved that addition of Si and Al to Fe significantly increased resistivity while maintaining soft magnetic properties [14]. Thus, ternary Fe-Si-Al alloys are reported to display attractive magnetic properties [[15], [16], [17], [18], [19]]. A well-known ternary alloy is Sendust (Fe-9.6Si-5.4Al). Although it is brittle, it is known for its soft magnetic behavior; the anisotropy constant K_1 and magnetostriction constants, λ_{100} and λ_{111}, all approach a zero value at this composition [20]. Fe-Al alloys are ductile even at concentrations of 7 to 8 % Al when there is partial ordering of the phases. However, with Al concentration of ~10 %, the deleterious effect of increased magnetostriction dominates [20]. For this ternary alloy system, both the magnetic and the electrical properties strongly depend on the composition and phase constitution.

Spark plasma sintering (SPS) is a rapid processing technique due to its fast sintering and high densification. It can be utilized to quickly prepare multiple alloy compositions, stacked one on top of another, in a single sample for materials discovery studies [21,22]. This high throughput SPS technique was used by passing a high electric current across a graphite die which is under pressure. The die is filled with powder, the current leads to heating and consolidation of the powder into a compact sample [[21], [22], [23], [24], [25]]. Brittle alloys can be readily prepared by this method.

Hence, a non-equilibrium processing route based on mechanical alloying, followed by spark plasma sintering (SPS), was utilized and a materials library of Fe-xSi-yAl alloys was developed. Mechanical alloying of Fe-Si resulted in nanosized particles of high Si content alloys which can lead to improved material properties [10]. For the ternary alloy compositions, the Si content was varied from 3 % (currently used Fe-Si binary alloys) to 9 %. Some compositions were selected to be like the composition range of Sendust alloys.

In this work, an accelerated methodology study was conducted to identify potentially promising novel materials compositions from a set of Fe-xSi-yAl ($x = 3, 7, 9; 0 \le y \le 8$) alloy compositions. Alloy powders, synthesized by mechanical alloying followed by high throughput spark plasma sintering, were consolidated to fabricate a multiple composition materials library bulk sample. The phases present, and the corresponding magnetic, mechanical, and electrical properties were then rapidly determined for each of the compositions in this materials library sample. Thus, the discovery of new materials of high industrial interest can be facilitated by such methods [12,21,22,[26], [27], [28], [29], [30], [31], [32], [33], [34]].

2. Experimental details

Powders of the relevant composition were prepared by a powder metallurgy method. High purity Fe (99.9 %), Si (99.9 %) and Al (99.9 %) powders from TOSOH SMD were mechanically alloyed in a high energy planetary ball mill (Fritsch Pulverisette 7 planetary micro mill). The vials were loaded with fifteen 10 mm diameter tungsten carbide balls and 15 g total weight of powder. 1 ml absolute ethanol was added to the powders as a control agent during high energy ball milling. Each cycle of milling was for 10 min, followed by a pause of 10 min to avoid excessive heating during milling. The total milling time of the samples was 5 h. Three sets of powders (Fe-3Si-yAl, Fe-7Si-yAl and Fe-9Si-yAl), each consisting of 9 different powder compositions (y ranging from 0 to 8), were prepared by this process.

Compositionally graded samples of ternary (i.e., $y = 1$ to 8) and binary (i.e., $y = 0$) alloys were prepared, at a vacuum level better than 8 Pa using a SPS equipment (Fuji Electronic Industrial, SPS-211LX). Various compositions of the mechanically alloyed alloy powders were placed one on top of another to form distinct layers in a 15 mm inner diameter, 60 mm height graphite die. These layers were separated from one another by Ta foils. The powders were consolidated into a single compositionally graded cylindrical sample, each such cylinder was a materials library.

After loading the graphite punch-and-die unit into the SPS chamber, both punches were connected to electrodes *via* graphite protection plates. During the sintering process, the sample was compressed at a pressure of 40 MPa and heated by Joule heating by means of the passage of direct current (DC). The samples were sintered at 950 °C for 15 min, followed by cooling to room temperature (RT) in the SPS chamber. To avoid thermal overshoot, a heating rate of 75 °C/min from RT to 900 °C and a heating rate of 17 °C/min from 900 to 950 °C was utilized. The samples were then vertically sliced, and characterization and property evaluation were carried out. Another sample set was heat treated at 1100 °C in a 5 % H_2+Ar gas mixture for 10 h, followed by characterization. Heat treatment in such a reducing gas can remove impurities and improve the magnetic properties [35].

X-ray diffraction (XRD) was conducted at room temperature using a Bruker D8 Discover diffractometer for compositionally graded samples, and Bruker D8 Advance for validation samples, employing Cu K_α radiation (λ = 0.15405 nm) over a range of 2θ = 20°–90°. The operating voltage and current were 40 kV and 40 mA, respectively. Phase identification was done using the software "Match! 3". Electron microscopy studies, elemental mapping and electron backscatter diffraction (EBSD) imaging were performed on a JEOL JSM-7800F PRIME field emission scanning electron microscope (FESEM), with attached Aztec – Ultim Max 170 mm^2 energy dispersive X-ray (EDX) spectrometer and Symmetric EBSD detector. Grain size observation was *via* Inverse pole figure (IPF) maps obtained at a step size of 0.05–0.1 μm in EBSD, using the area-weighted mean values. The microhardness was measured at a load of 1 kgf using a Vickers hardness tester (Future-Tech). A four-point probe tester (Keithlink) was used to determine the electrical resistivity of each composition.

Magnetic characterization was performed on similarly sized samples, using a Lakeshore 7400 vibrating sample magnetometer (VSM) for magnetic fields up to 14.5 kOe. The Curie temperature for selected samples were determined using an in-lab developed method using a thermogravimetric analysis (TGA, TA Instruments Q600 SDT) instrument and a permanent magnet [26], while the densities of the validation samples were measured via the Archimedes method. The densities of compositionally graded samples were not measured as each sample contained multiple compositions and a Ta foil spacer between each layer. Ta has a density approximately double that of Fe and will interfere with density calculations.

A schematic of the high throughput process is shown in Fig. 1.

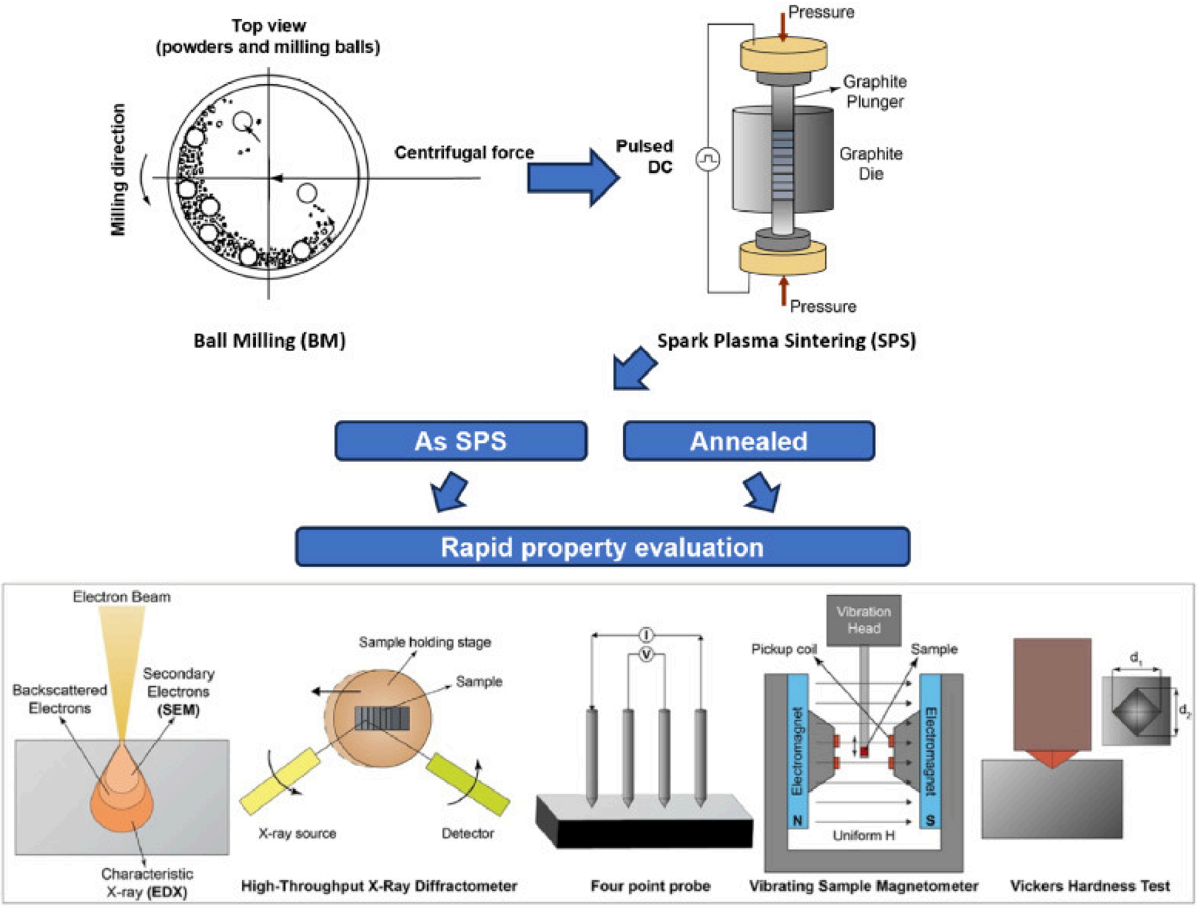

1. Download: Download high-res image (655KB)
2. Download: Download full-size image

Fig. 1. A schematic of the ball milling process [36], the SPS process for compositionally graded Fe-xSi-yAl alloys with Ta foil between the layers, and the techniques used for rapid property evaluation [37].

3. Results and discussion

3.1. Phase identification

Fig. 2a shows the reported phase diagram of Fe-Si [38,39]. The predicted BCC/B2 phase transition of the synthesized Fe-xSi-yAl alloy library compositions with respect to temperature using the TCHEA4 database is shown in Fig. 2b. Compared to the reported phase diagram of binary Fe-Si in Fig. 2a, the D03 phase is not present in the ternary system for the compositions of interest in Fig. 2b.

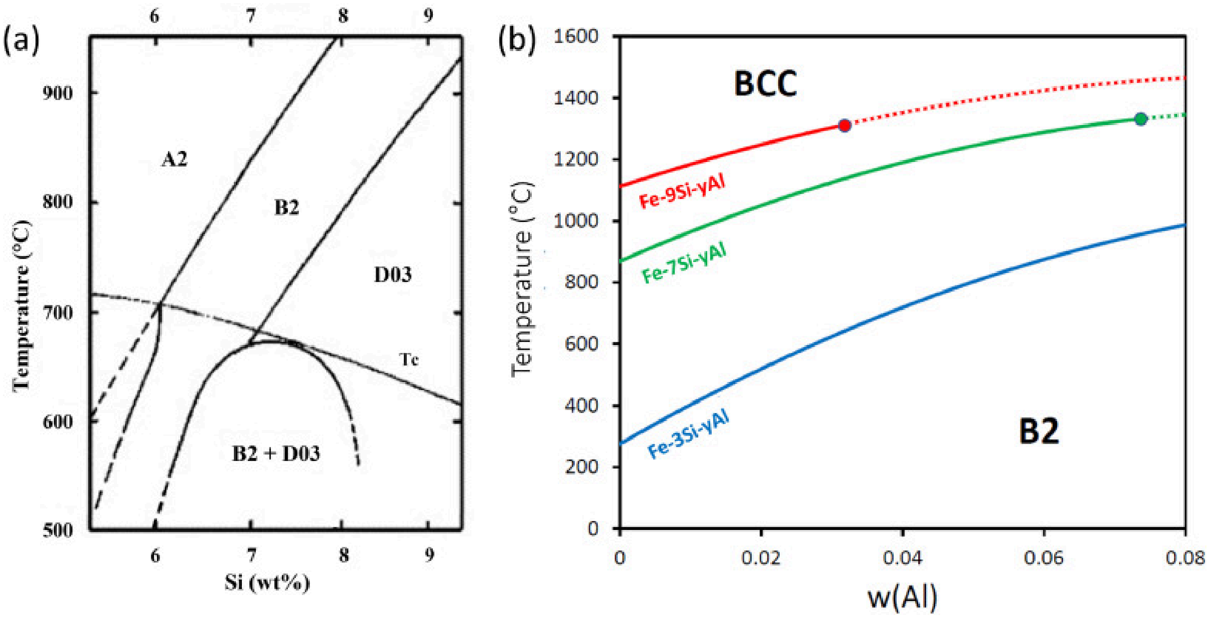

1. Download: Download high-res image (437KB)
2. Download: Download full-size image

Fig. 2. (a) Binary phase diagram of Fe-Si [38,39] and (b) BCC to B2 transition as a function of temperature and composition of the ternary Fe-xSi-yAl alloys.

After compaction by SPS at 950 °C and heat treatment at 1100 °C, the predicted changes in phase fraction of the BCC/B2 in the ternary alloy is shown in Fig. 3a and b, also predicted using the TCHEA4 database. The stability of the B2 phase increases with higher Si and Al concentrations. The B2 phase is known to be beneficial for improving M_s, but it can decrease the mechanical properties [3].

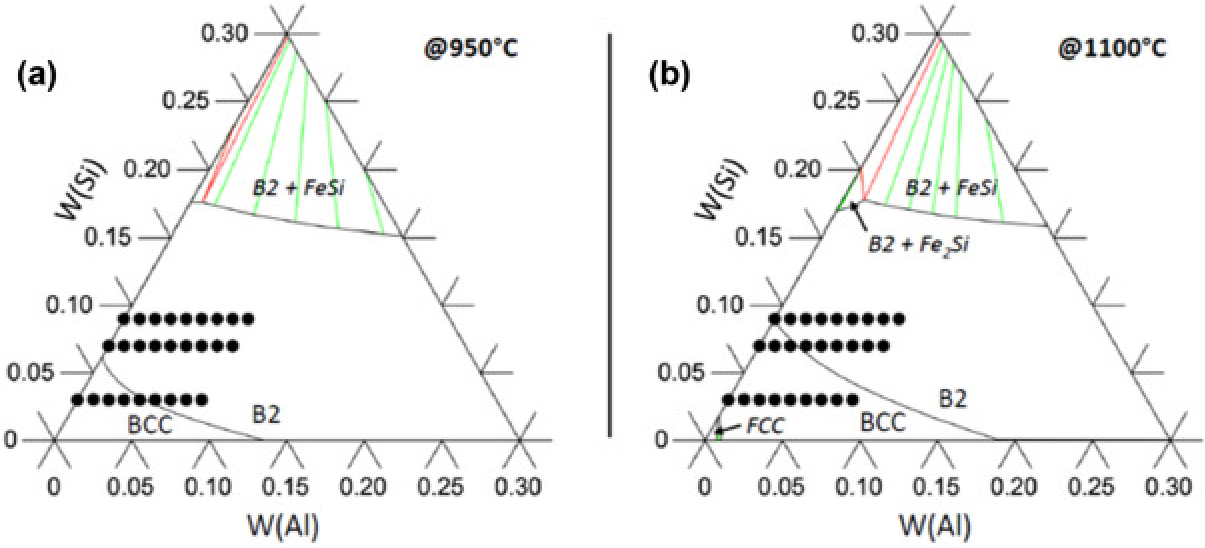

1. Download: Download high-res image (261KB)
2. Download: Download full-size image

Fig. 3. Boundary of the BCC/B2 phase transition with composition at different temperatures: (a) 950 °C and (b) 1100 °C. Black dots correspond to the alloy compositions reported in this work.

The composition of the as SPS Fe-xSi-yAl alloy samples are shown in Table S1 in the Supporting Information (SI). The XRD patterns of the as SPS and after heat treatment Fe-xSi-yAl alloy materials library samples are shown in Fig. S1 in SI. For the 3 sets of as SPS materials libraries, the α-Fe-Si or α-

Fe-Si-Al BCC crystal structures were identified from the 110, 200 and 211 diffraction peaks. Minor diffraction peaks from the Ta foil were also observed at ∼38°. The binary alloys (*y* = 0) generally exhibited low intensity diffraction peaks.

After heat treatment, the peak intensities of the binary alloy samples increased significantly, while the XRD patterns of the other Al-containing compositions did not exhibit much change. The alloys exhibited a single BCC phase both before and after heat treatment. The diffraction peaks were more pronounced after heat treatment possibly due to grain growth and increase in crystallinity.

The XRD patterns of the alloy compositions exhibited a single-phase BCC structure, and not the B2 phase, possibly due to such peaks being low in intensity, below the detectability limit of the diffractometer [40]. Other reports of ball milled Fe-Si, Fe-Si-Al or Sendust alloys [10,[41], [42], [43], [44]] also report an absence of the B2 and/or the D03 peaks for samples processed under similar conditions. The D03 phase is reported to form in processes involving low cooling rates [45].

3.2. Magnetic properties

Fig. 4 shows the variation of saturation magnetization (M_s) and coercivity (H_c) with alloy composition in a contour plot for as SPS and heat treated samples. Calculated relative permeability values for these alloys are shown in SI Table S2. In Fig. 4a, the M_s values of as SPS samples are in the range of 122 to 196 emu/g, with M_s varying from Fe-3Si-yAl (highest Fe content values) to Fe-9Si-yAl (lowest Fe content values). There was some deviation from the general trend in the region at Al = 3 wt%, possibly due to the non-equilibrium state of the sample: the SPS duration was short, and the samples cooled down rapidly. H_c (Fig. 4b) ranged from 17 to 39 Oe and exhibited high values in the Fe-rich regions. The lowest H_c values were observed for Fe-9Si and Fe-7Si-6Al.

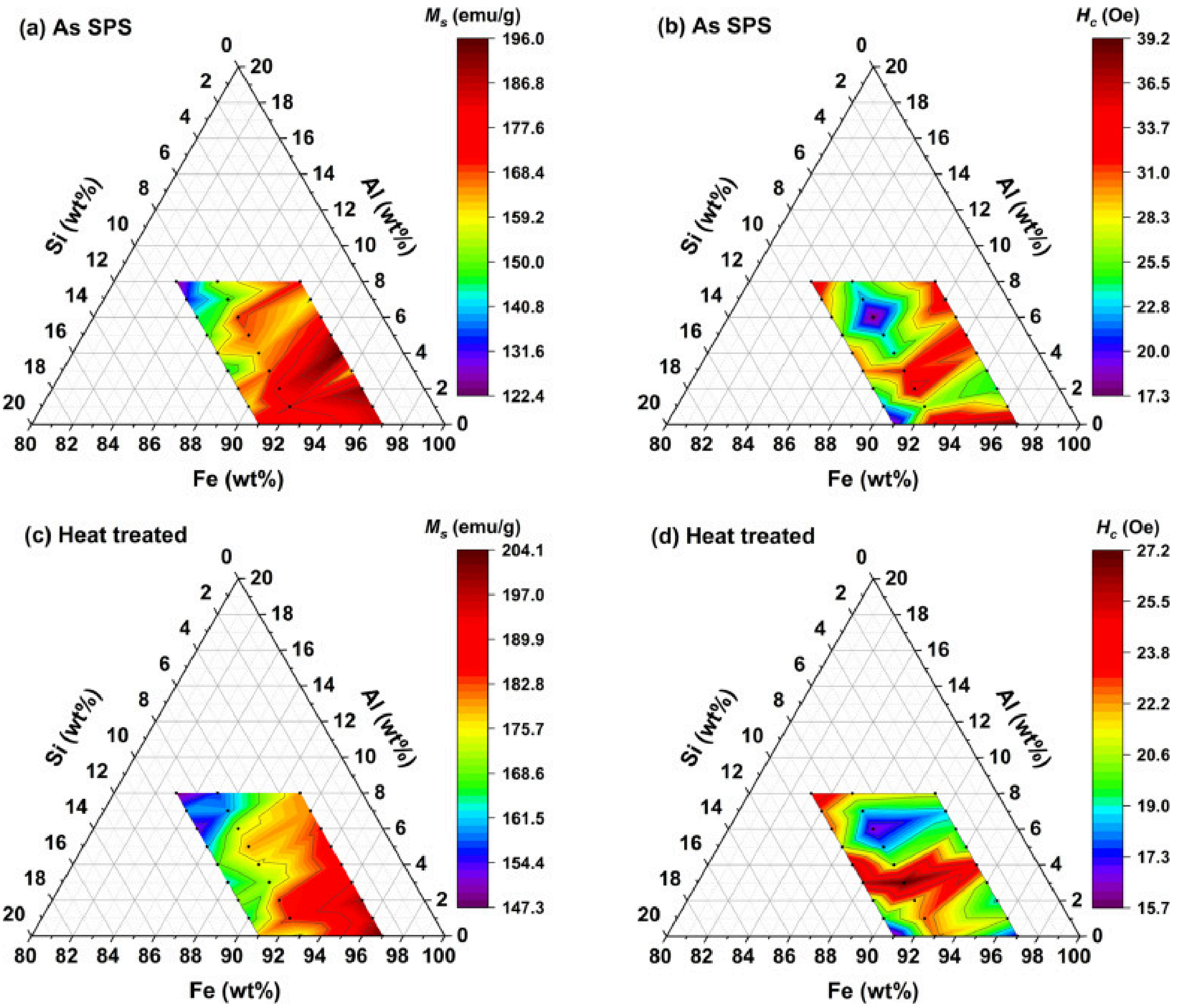

1. Download: Download high-res image (1MB)
2. Download: Download full-size image

Fig. 4. The saturation magnetization, M_s, and coercivity, H_c, of (a, b) as SPS and (c, d) heat treated Fe-xSi-yAl alloy samples as a function of composition.

After heat treatment (Fig. 4c), the M_s values were in the range of 147 to 204 emu/g, with a clear trend of M_s for the alloys: M_s decreased with higher Si content. For the same Si content, M_s further decreased monotonically for larger Al content.

The M_s of the heat treated Fe-9Si-6Al sample was ~152 emu/g, comparable to the maximum M_s of ~156 emu/g obtained for mechanically alloyed, cold pressed Sendust powder [40]. The M_s of heat treated Fe-7Si was ~175 emu/g, slightly lower than that of the Fe-6.5Si powders, which was ~188 emu/g [46]. The M_s of the heat treated Fe-9Si sample was ~178 emu/g, close to the 175 emu/g possessed by Fe-10Si powders [10]. These M_s values are comparable to those reported in literature for powder or cold pressed samples thus there is no adverse effect of heat treatment and density of samples on the magnetic properties.

In general, the results showed that alloys with higher Si content had lower saturation magnetization. This could be due to a smaller number of unpaired 3*d* electrons of the Fe atoms due to the increased concentration of diamagnetic Si atoms with 2p electrons [47]. The decrease in M_s with increased Al content is due to the interaction of the 3*d* electrons of the Fe atoms with the 2*p* electrons of the paramagnetic Al atoms [47].

The H_c values after heat treatment (Fig. 4d) decreased to between 15.7 to 27.2 Oe. There was no clear trend of H_c with composition, but ternary Fe-9Si-yAl exhibited relatively higher values, while Fe-7Si-6Al, Fe-9Si and Fe-3Si possessed the lowest H_c values. The reported H_c values of mechanically alloyed Sendust [18,43] and gas atomized Fe-6.5Si powders [46] were ~4 Oe and ~13.6 Oe, respectively. The higher H_c values of as SPS samples were attributed to internal strain and stress induced by the mechanical alloying and the compaction process in SPS respectively, which can be relieved by heat treatment [41,42,48].

Fig. 5 shows the Curie temperature (T_c) of the three as SPS binary Fe-Si alloys and selected as SPS Fe-xSi-yAl ternary alloys with respect to composition. The range of values were from ~759 °C for Fe-3Si to ~636 °C for Fe-9Si-8Al. T_c decreased with higher Si content. The trend is expected; T_c is a function of the effective exchange interaction of the elements Fe, Si and Al [49,50]. Si is diamagnetic and Al is paramagnetic, hence the effective exchange interaction is expected to decrease with higher content of Al and Si.

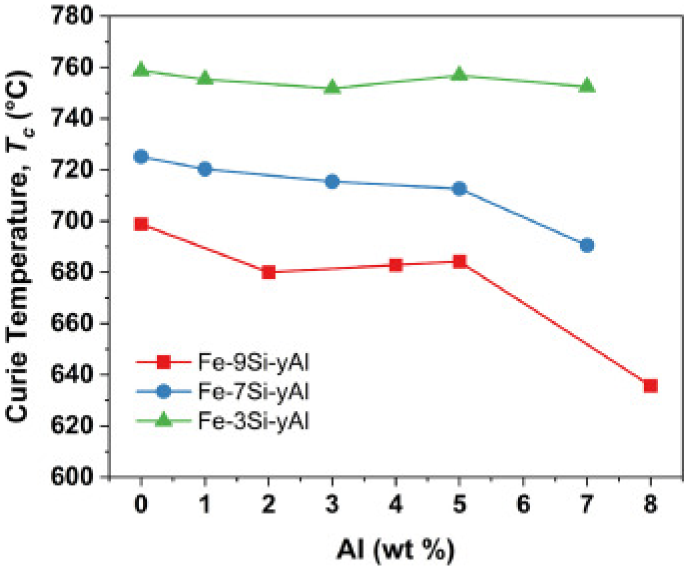

1. Download: Download high-res image (184KB)
2. Download: Download full-size image

Fig. 5. Curie temperature, T_c, of as SPS binary Fe-Si and selected as SPS Fe-xSi-yAl ternary alloys with respect to composition.

3.3. Electrical resistivity and hardness

The electrical resistivity values of as SPS Fe-xSi-yAl alloys are presented in Fig. 6a. Fe-9Si-yAl alloys exhibited superior resistivity values compared to Fe-7Si-yAl and Fe-3Si-yAl alloys due to the higher Si wt%. In these three materials series, the electrical resistivities increased with higher Al content. The highest value of 272 μΩ.cm was obtained for Fe-9Si-8Al, while the lowest value of 60.6 μΩ.cm was obtained for Fe-3Si-1Al.

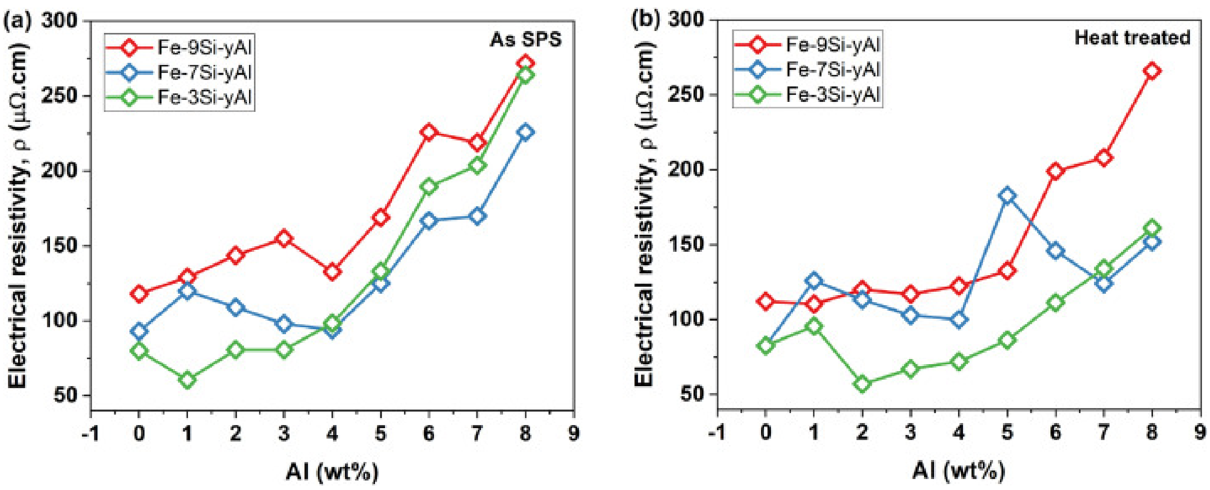

1. Download: Download high-res image (509KB)
2. Download: Download full-size image

Fig. 6. Electrical resistivity, ρ, of Fe-xSi-yAl alloys (a) as SPS and (b) heat treated samples as a function of Al wt%.

After heat treatment (Fig. 6b), the highest value of resistivity obtained remained that for Fe-9Si-8Al (266 μΩ.cm), but the lowest value was now observed in Fe-3Si-2Al (57 μΩ.cm).

The magnitude of the change in electrical resistivity was a function of the alloy composition: For Fe-3Si-yAl, it increased ~3 % and 58 % for $x = 0$ and 1, it decreased between 17 % and 41.2 % for $x = 2$ to 8, respectively. For Fe-7Si-yAl, the values increased between 3.8 % to 46 % for $x = 1$ to 5, while they decreased for $x = 0$, and 6 to 8 by between 11.2 % to 32.7 %. For Fe-9Si-yAl, all compositions exhibited a decrease in resistivity between 2.2 % to 24.5 % after heat treatment.

The changes in resistivity after heat treatment could be due to strain / stress relief or the removal of impurities, like surface oxides, in the alloy. Fe has an electrical resistivity of 10 μΩ.cm [51], while the values for Fe-3Si, Fe-7Si and Fe-9Si are 45, 85 and 96 μΩ.cm respectively [7]. The values of our Fe-3Si, Fe-7Si and Fe-9Si alloys were found to be 83, 83 and 112 μΩ.cm, respectively. These resistivity values were similar or higher than the reported values in the literature for similar compositions. The electrical resistivity value of as SPS Fe-3Si was only slightly lower than that of Fe-7Si, and after heat treatment, both samples had similar values.

The electrical resistivity value for a composition close to Fe-9Si-8Al and for Fe-3Si-2Al was reported to be 120 μΩ.cm and ~60 μΩ.cm, respectively [7]. The resistivity value obtained in this work for Fe-3Si-2Al was close to the reported value. However, the electrical resistivity value for Fe-9Si-8Al (~266 μΩ.cm) obtained in this work was more than twice the reported value. Mechanically alloyed powders have more interfaces and other defects compared to cast alloys, leading to more electron scattering and higher resistivity. The increase in electrical resistivity can also be attributed to significant local lattice distortion due to the large atomic size mismatch of Al with the other alloy components, resulting in increased electron scattering and a lower mean free path [47]. In addition, the trends of the electrical resistivity of the different sets of ternary alloys show some overlapping or crosses one another due to possible localised differences, e.g., in the phases present, or due to the mechanical alloying and subsequent processing. Fe-9Si-yAl (in Fig. 3) was predicted to remain in a single-phase region at the different processing temperatures, hence it does not show as much variation.

Fig. 7 shows the Vickers hardness of the alloys as a function of Al content. The range of microhardness values (Fig. 7a) for as SPS ternary Fe-9Si-yAl and Fe-7Si-yAl are 337–465 HV and

345–492 HV respectively, while the range for Fe-3Si-yAl is lower at 192 to 369 HV.

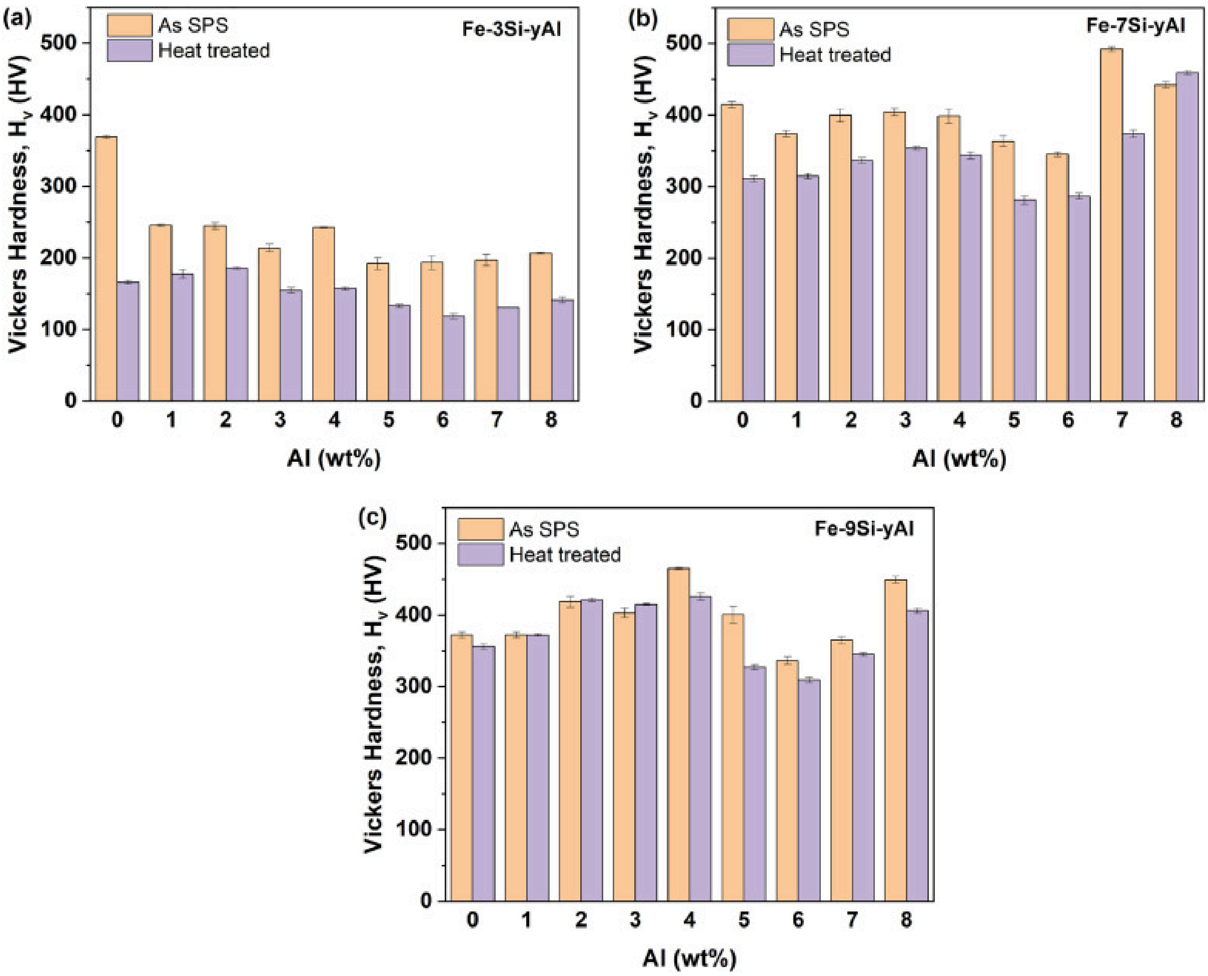

1. Download: Download high-res image (724KB)
2. Download: Download full-size image

Fig. 7. Vickers hardness, H_v, of (a) Fe-3Si-yAl, (b) Fe-7Si-yAl and (c) Fe-9Si-yAl alloys as a function of Al wt%.

After heat treatment (Fig. 7b), apart from some compositions exhibiting a minor increase in hardness of 0.6–4 %, the microhardness values in general decreased by ~0.1–18 %, 12.5–25 %, and 24–55 % for Fe-9Si-yAl, Fe-7Si-yAl and Fe-3Si-yAl, respectively. The general trend is that microhardness increased with higher Al content, dipped slightly at Al = 5–6 %, and increased subsequently. The decrease in hardness after heat treatment is likely to be due to the reduction of defect content as well as grain growth, as confirmed by the sharper diffraction peaks in the XRD patterns (Fig. S1). The hardness of pure Fe is ~62 HV [52]; adding Si and Al improves hardness significantly due to solid solution hardening – Fe-xSi-yAl formed a single BCC phase, as seen in the XRD patterns.

Of the 3 ternary alloy systems, Fe-3Si-yAl exhibits the largest change in microhardness values. This may be due to the absence of B2 phase after heat treatment, as predicted in Fig. 2, while for the Fe-7Si-yAl and Fe-9Si-yAl sets of alloys, 4 compositions (Fe-7Si, Fe-9Si, Fe-7Si-1Al and Fe-7Si-2Al) out of the 18 compositions in the series were predicted to exhibit an absence of the B2 phase. However, based on Fig. 7 and the percentage change calculations in SI Table S3, nine of the eighteen Fe-7Si-yAl and Fe-9Si-yAl alloy compositions experienced a double digit% change in microhardness. This deviation from the predictions of Fig. 2 might be due to a shift in the phase boundary due to the non-equilibrium nature of ball milling synthesis and subsequent processing conditions.

From the results, the alloys with 7 % and 9 % Si exhibit higher microhardness values compared to 3 % Si; the compositions with the highest microhardness values were Fe-9Si-4Al and Fe-7Si-8Al at ~426 HV and ~460 HV. To correlate these results to the presence of the BCC and B2 phases, based on Fig. 2, the compositions with 7 % and 9 % Si are predicted to have more B2 content, which is reported to be an ordered phase which restricts dislocation motion, resulting in the observed higher hardness. Hardness values are used as a proxy to indicate how strong the Fe-xSi-yAl alloys are, as these values are usually well correlated to tensile strength and yield strength values. The microhardness values can also be compared with commercially used alloys.

Boulouma et al. reported [53] that the microhardness of arc melted Fe-3.4Si-6.4Al was 43 HV, while that of Fe-6.3Si-6.2Al was 52 HV and the value for Sendust (Fe-9Si-6Al) was ~70 HV. Melt spun Fe-6.5Si ribbons prepared at various wheel speeds possessed hardness in the range of 529–573 HV [54], while a magnetron sputtered commercial sheet had a hardness of ~325 HV for the Fe-5.4Si composition [55]. Thus, as expected, different processing conditions can alter the hardness values.

3.5. Validation

The radar plots for compositions versus the normalized material properties for the three sets of alloys are shown in Fig. 8a–c. From each of the plots, promising compositions exhibiting the best M_s, lowest H_c, highest electrical resistivity and microhardness (i.e., values closest to 1) were identified – resulting in a total of 10 compositions. The as-measured material properties of these 10 compositions were then compared and normalized once more before being plotted together in Fig. 8d. From Fig. 8d, 4 compositions exhibiting the best M_s, lowest H_c, highest microhardness and electrical resistivity were selected. The compositions are Fe-3Si, Fe-9Si, Fe-7Si-8Al and Fe-9Si-8Al, and they are highlighted in Fig. 8d using bold lines.

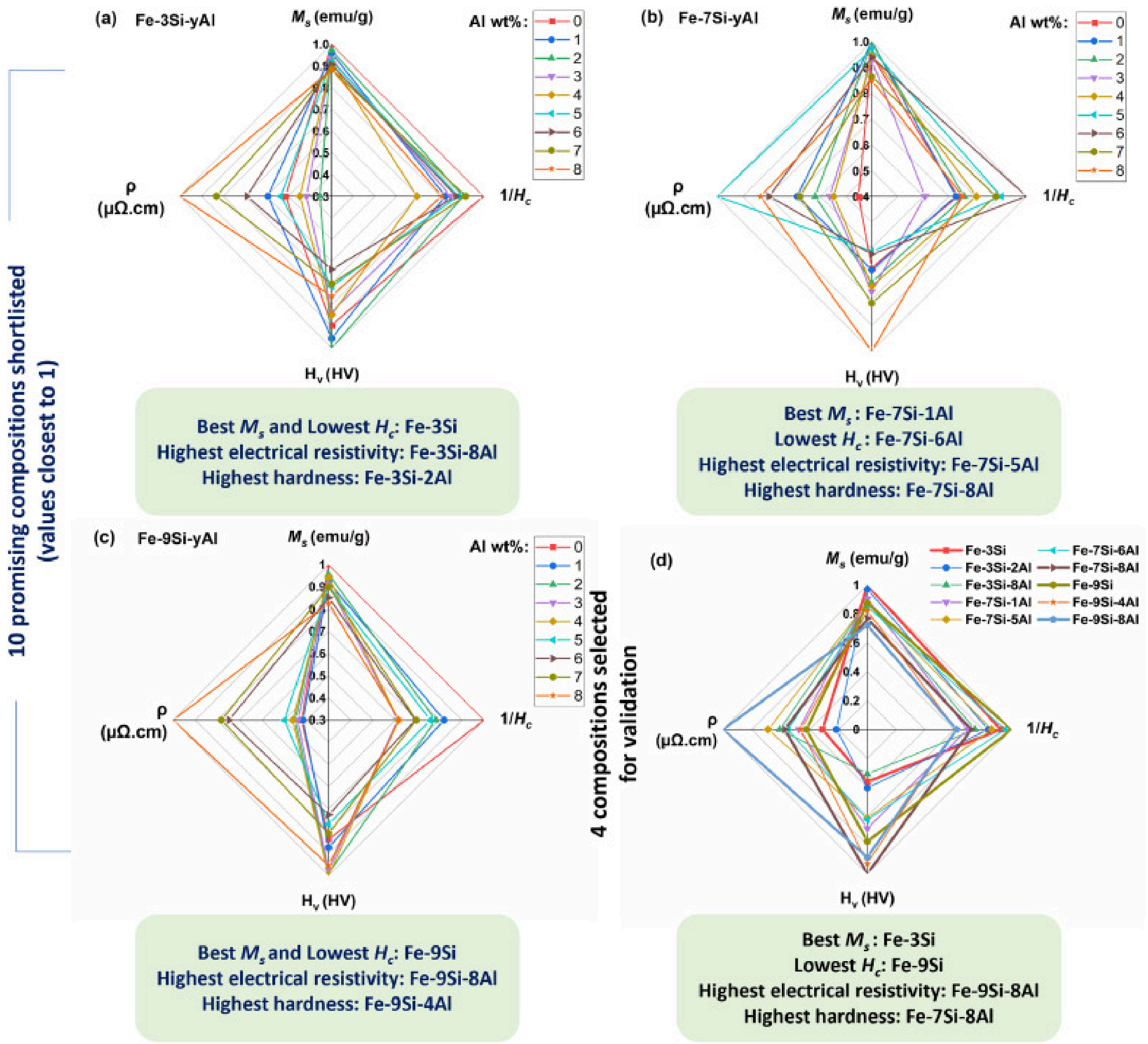

1. Download: Download high-res image (2MB)
2. Download: Download full-size image

Fig. 8. Radar plot of M_s, $1/H_c$, H_v and ρ of (a) Fe-3Si-yAl, (b) Fe-7Si-yAl and (c) Fe-9Si-yAl as a function of Al wt%. (d) Comparison of the 10 promising compositions from different alloy sets, with the 4 compositions selected for further validation (shown as bold lines).

These 4 compositions were individually prepared under the same processing conditions (SPS and heat treatment) as the compositionally graded samples, and the material properties were then validated. The measured densities of the as SPS validation samples ranged from 83–91 % of the theoretical density. The overall compositions of the as SPS samples were measured using EDX and shown in Table 1.

Table 1. EDX Compositions of as SPS validation samples.

Compositions	**Al (wt%)**	**Si (wt%)**	**Fe (wt%)**
Fe-3Si	–	4.02	95.98
Fe-7Si-8Al	9.55	6.56	83.89
Fe-9Si	–	9.89	90.11

Compositions	Al (wt%)	Si (wt%)	Fe (wt%)
Fe-9Si-8Al	9.25	8.38	83.27

The actual compositions deviated slightly from the nominal compositions due to the nature of the mechanical alloying process. However, the values are within ±1 % Si for all alloys, and for the ternary alloys, Al is within 1.6 %.

The measured material properties from high throughput experiments (HTP) compared to validation samples (VS) are plotted in Fig. 9.

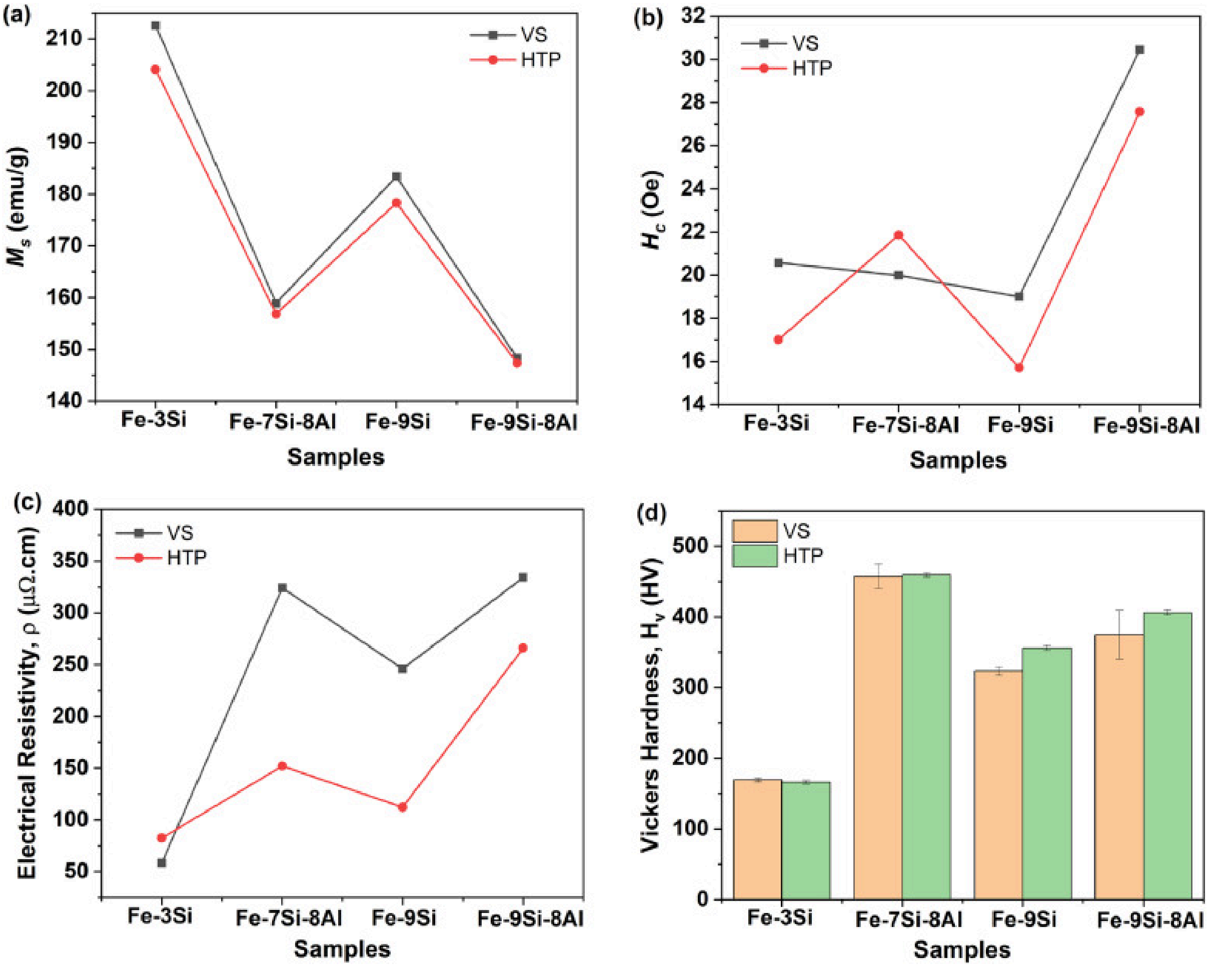

1. Download: Download high-res image (748KB)
2. Download: Download full-size image

Fig. 9. Comparison of material properties of validation samples (VS) with samples from high throughput (HTP) experiments: (a) Saturation magnetization, M_s, (b) coercivity, H_c, (c) electrical resistivity, ρ and (d) Vickers hardness, H_v.

As seen in Fig. 9a, the M_s of both sets of samples match closely. In Fig. 9b, the lowest H_c was still obtained in the Fe-9Si sample, although the absolute value (~19 Oe) was about 21 % higher than that from HTP experiments (15.7 Oe). Other than Fe-7Si-8Al, the trend of variations in H_c are similar. The different H_c values may be due to localised changes in the SPS processing in the HTP and validation cases, as H_c is known to be sensitive to processing [37].

Due to the localised differences in SPS processing condition in HTP and validation experiments (i.e., compositionally graded vs single composition), some difference in density is expected. Its effect on M_s, however, is small in our findings.

In Fig. 9c, the electrical resistivities of the validation samples were about 1.25 times to 2.2 times higher than the HTP samples. An exception is the Fe-3Si sample, whose resistivity was ~30 % lower than the HTP samples. The highest resistivity value was obtained in the Fe-9Si-8Al sample, as also observed in the HTP experiments. However, it was only about 3 % higher than the Fe-7Si-8Al sample, the composition with the next highest resistivity value, unlike in the HTP experiments, where the value for Fe-9Si-8Al was 75 % higher than that of Fe-7Si-8Al. In general, for HTP compositionally graded SPS samples, the density should be lower than the validation samples, where single samples are processed. This should correlate to higher resistivity results in HTP samples. However, this is not the case. Hence, the density differences between VS and HTP samples do not play a significant role in our results.

The microhardness of the samples is shown in Fig. 9d. HTP samples exhibited either similar or slightly higher values than validation samples, and the trend across the samples were similar. The highest microhardness values were achieved in Fe-7Si-8Al for both HTP and validation experiments. The potential effect of density differences was not significant. Thus, from the observations of electrical resistivity and microhardness changes, it is possible that microstructural or compositional effects are the contributing factors, as discussed next.

Comparing the material properties of the 4 validation samples in a tabular form (Table S4 in SI), 2 compositions, Fe-7Si-8Al and Fe-9Si, gave the most promising combination of properties. Thus, further microstructural and compositional investigations *via* EBSD and EDX were done for the heat treated HTP and VS samples for these 2 compositions.

The EBSD results (band contrast images and out-of-plane crystallographic texture maps) are shown in Fig. 10. In general, from band contrast images in Fig. 10a–d, porosity remained comparable between both the HTP and validation samples, confirming our earlier hypothesis that there are no density differences affecting the material properties. There were, however, some black impurities observed on the surfaces and some dark region between the grains of the Fe-9Si samples in Fig. 10b and d. The black impurities may be silica residue from the polishing step, and the dark region may be the gaps between the grains or some very fine-nanosized grains from the ball milling process, difficult to index *via* EBSD at the current step size used [56]. Hence, they were reflected as zero solutions (i.e., white regions) in the texture maps from Fig. 10e–h, as they were not indexed in EBSD. The zero solutions areas in HTP samples are smaller than in the VS cases, which may be due to the differences in the processing. Crystallographic texture maps highlight the random grain orientation of SPS samples induced by the high energy ball milled powder and sintering mechanism.

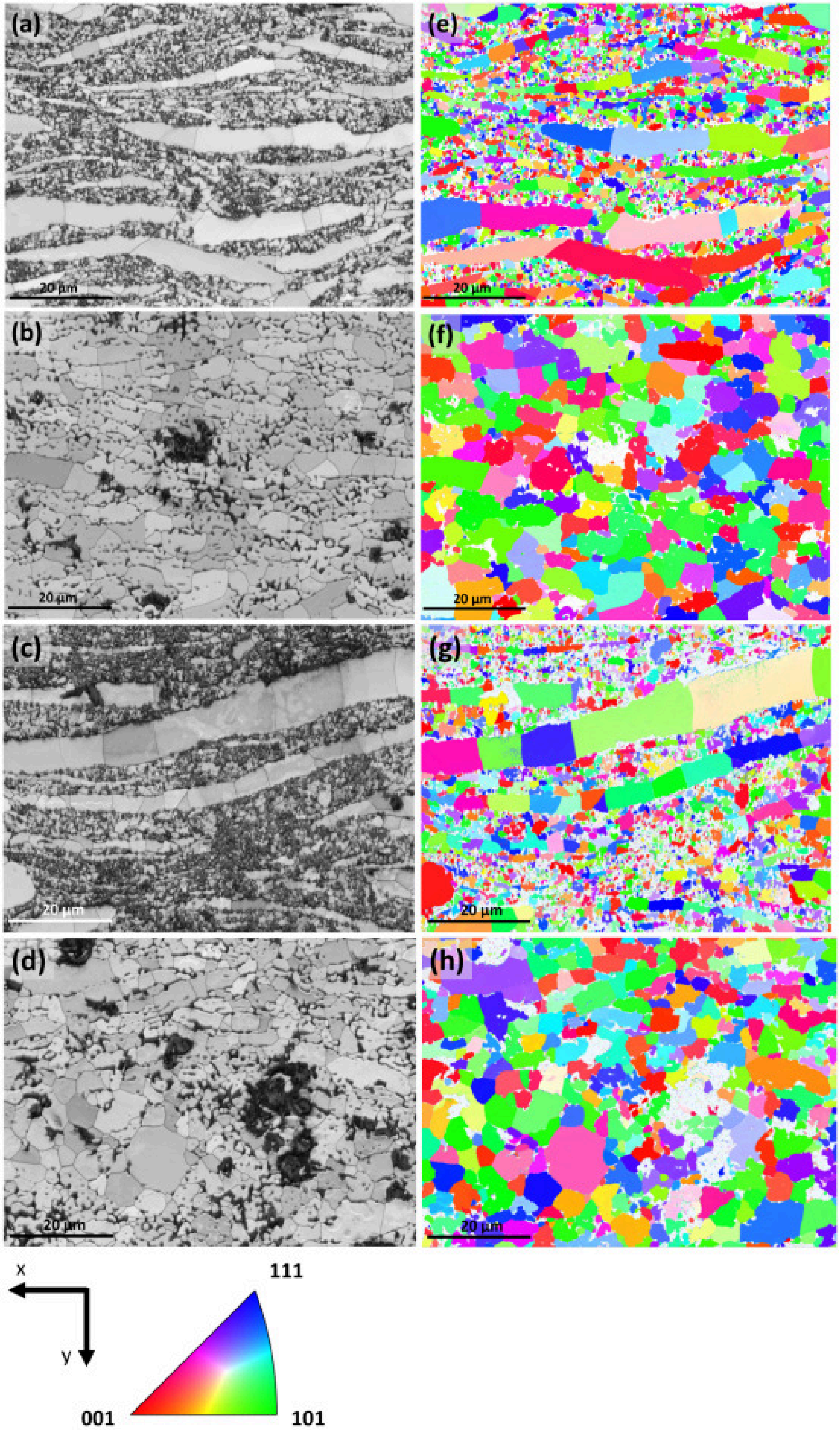

(a)
20 µm
(e)
20 µm
(b)
20 µm
(f)
20 µm
(c)
20 µm
(g)
20 µm
(d)
20 µm
(h)
20 µm
x
y
111
001
101

1. Download: Download high-res image (3MB)
2. Download: Download full-size image

Fig. 10. EBSD band contrast and crystallographic texture maps at 1500x magnification of heat treated high throughput (a, e) Fe-7Si-8Al, (b, f) Fe-9Si, and validation samples (c, g) Fe-7Si-8Al, (d, h) Fe-9Si.

The grain sizes and its distribution are shown in Table 2. From Fig. 10 and Table 2, binary composition contained grain sizes which are more regularly shaped, with an average size ranging from ~4.77 to 5.89 μm, while ternary composition exhibited bi-modal grains which are large, longitudinally-shaped and much smaller, regularly shaped, in the range of ~4.74–4.82 μm and ~1.03–1.07 μm respectively. In terms of processing, both HTP and validation samples had similar microstructures which were composition dependent, but there was some variation in the grain sizes, especially for Fe-9Si.

Table 2. Grain size distribution of high throughput and validations samples of Fe-7Si-8Al[^] and Fe-9Si (taken from image at 500x magnification).

Samples	**Counts**	**Area weighted mean (μm)**
HTP Fe-7Si-8Al	7358	1.07
	3685	4.82
VS Fe-7Si-8Al	**994**	**1.03**
	3247	**4.74**
HTP Fe-9Si	2795	5.89
VS Fe-9Si	**4232**	**4.77**

^

Fe-7Si-8Al has bi-modal grain size distribution, hence there are 2 rows shown.

More in-depth investigation *via* EDX was carried out to identify the phases. The results showed that there were some localised compositional differences (Fig. S2, S3 and Table S5 in SI). These compositional differences are expected to have contributed to the differences in electrical resistivity and coercivity, while saturation magnetization and hardness were less affected. The main phase was a Fe-Si phase with about 5–7 wt% Si, and a second binary or ternary phase, in Fe-9Si and Fe-7Si-8Al respectively. The significant difference in the composition of the ternary second phase of Fe-7Si-8Al in HTP and VS samples seems to suggest that processing can affect the final composition obtained.

The presence of these phases was confirmed by XRD patterns of validation samples, as SPS and after heat treatment, presented in Fig. 11a–b. All four samples crystallized mainly in the BCC structure corresponding to the 110, 200, 211 peaks. The 110 peaks for Fe-3Si and Fe-7Si-8Al are sharper and have higher intensity after heat treatment, while 110 peak of Fe-9Si and Fe-9Si-8Al do not show obvious differences.

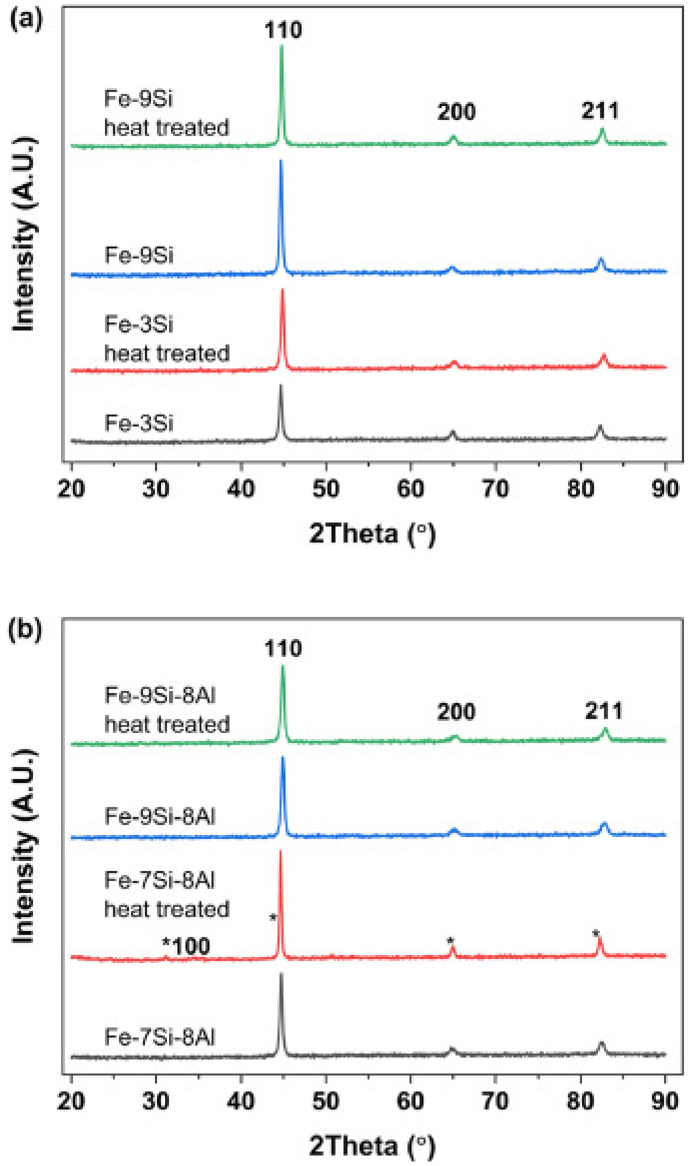

1. Download: Download high-res image (403KB)
2. Download: Download full-size image

Fig. 11. XRD patterns of the validation samples as SPS and heat treated (a) binary Fe-3Si and Fe-9Si and (b) ternary Fe-7Si-8Al and Fe-9Si-8Al.

For heat treated Fe-9Si, based on the EDX results, there were two BCC phases present – in the XRD patterns, they can be matched to the crystal structure of $Fe_{0.94}Si_{0.06}$ (PCPDF card no. 04–017–6672) and $Fe_{0.75}Si_{0.25}$ (PCPDF card no. 04–016–6263). For Fe-7Si-8Al, based on EDX results, the XRD patterns were matched to a BCC phase, $Fe_{0.94}Si_{0.06}$ (PCPDF card no. 04–017–6672), a ternary primitive phase, $Fe_{0.95}Al_{0.89}Si_{0.16}$ (PCPDF card no. 04–018–0311), consisting of an additional small 100 peak, with the other peak positions overlapping with the BCC phase peak positions, indicated by *). Based on its crystal structure information, this ternary phase should be a B2 phase [10,45]. Although the 100 peak position can exist in both B2 and D03 phase [3,57], as the characteristic 111 peak for D03 phase is absent, it is deduced that the ordered phase present is B2.

Even though there were two majority phases present, their peak positions were close to one another, hence in the XRD patterns, it appeared as a single phase, with the diffraction peaks appearing slightly broader (especially 200 and 211). The additional phase is now discernible, as another XRD machine was used for characterizing the validation samples. The absence of obvious B2 peaks in other compositions deviated from the thermodynamic calculations in Fig. 2, Fig. 3, where the B2 phase was expected in them. This deviation from the thermodynamic prediction versus the experimental results may be due to the non-equilibrium processing conditions, a short heat treatment time of 10 h was insufficient for it to reach equilibrium, and/or as highlighted earlier, due to the characterization equipment capability limitation.

From the above results, an attractive combination of properties was discovered in the novel heat treated Fe-7Si-8Al sample. The M_s was ~158.9 emu/g, H_c was ~20 Oe, resistivity was ~324 μΩ.cm and microhardness was ~457.5 HV. Higher resistivity and microhardness of Fe-7Si-8Al in comparison to Fe-3Si makes it favourable for use in high frequency applications. The above composition and phase information gives us an insight to the nature of the ternary alloys. Thus, this composition can be further explored and optimized for industrial applications.

4. Conclusions

Multiple properties of compositionally graded Fe-3Si-yAl, Fe-7Si-yAl, and Fe-9Si-yAl materials libraries (*y* = 0 to 8) prepared by mechanical alloying, high throughput spark plasma sintering and then heat treatment were rapidly assessed.

- 1.

All ternary alloys possessed a single-phase BCC structure. The composition with the highest M_s was Fe-3Si. The lowest H_c was obtained for Fe-9Si.

- 2.

The electrical resistivities increased with higher Si content and increased gradually with larger Al content. The highest value was obtained in Fe-9Si-8Al.

- 3.

Larger Si content samples had higher microhardness and adding different wt% of Al led to varying changes in microhardness. The highest value was obtained in Fe-7Si-8Al.

- 4.

Four promising compositions were identified based on the rapid characterization and property evaluation of the materials libraries. Validation studies showed that the sample with the composition Fe-7Si-8Al exhibited a relatively good M_s of ~158.9 emu/g, H_c of ~20 Oe, and the highest resistivity and microhardness of ~324 μΩ.cm and ~457.5 HV respectively.

Thus, our rapid methodology to evaluate multiple properties was successfully deployed to identify a potential novel ternary Fe-xSi-yAl alloy for energy applications.

CRediT authorship contribution statement

Zviad Tsakadze: Writing – original draft, Visualization, Methodology, Investigation. **Li Ping Tan:** Writing – review & editing, Writing – original draft, Visualization, Validation, Investigation. **Karl P. Davidson:** Writing – review & editing, Visualization, Investigation. **Stéphane Gorsse:** Resources, Formal analysis. **V. Chaudhary:** Writing – review & editing, Supervision, Methodology, Conceptualization. **R.V. Ramanujan:** Writing – review & editing, Supervision, Resources, Funding acquisition, Conceptualization.

Declaration of competing interest

The authors declare that they have no known competing financial interests or personal relationships that could have appeared to influence the work reported in this paper.

Acknowledgements

We would like to acknowledge the support of the Production Area of Advance (AoA) at Chalmers

University of Technology, and the Facility for Analysis, Characterization, Testing and Simulation (FACTS) at Nanyang Technological University for the use of their electron microscopy and X-ray facilities.

Funding

This work was supported by the AME Programmatic Fund by the Agency for Science, Technology and Research, Singapore under Grant No. A1898b0043 and A18B1b0061.

Appendix. Supplementary materials

Download: Download Word document (4MB)

References

1. [1]

V. Chaudhary, S.A. Mantri, R.V. Ramanujan, R. Banerjee
Additive manufacturing of magnetic materials
Prog. Mater. Sci., 114 (2020), Article 100688, 10.1016/j.pmatsci.2020.100688
View PDFView articleView in ScopusGoogle Scholar

2. [2]

A. Renuka Balakrishna, R.D. James
Design of soft magnetic materials
NPJ Comput. Mater., 8 (2022), p. 4, 10.1038/s41524-021-00682-7
View in ScopusGoogle Scholar

3. [3]

G. Ouyang, X. Chen, Y. Liang, C. Macziewski, J. Cui
Review of Fe-6.5 wt%Si high silicon steel—a promising soft magnetic material for sub-kHz application
J. Magn. Magn. Mater., 481 (2019), pp. 234-250, 10.1016/j.jmmm.2019.02.089
View PDFView articleView in ScopusGoogle Scholar

4. [4]

K. Aiso, K. Akatsu
Performance comparison of high-speed motors for electric vehicle
World Electric Veh. J., 13 (2022), p. 57, 10.3390/wevj13040057
View in ScopusGoogle Scholar

5. [5]

K. Byerly, S. Simizu, M.E. McHenry, P.R. Ohodnicki, R.B. Beddingfield, S. Bhattacharya, G. Nojima
Permeability engineered soft magnetics for power dense energy conversion
2021 IEEE Energy Conversion Congress and Exposition (ECCE) (2021), pp. 5320-5326, 10.1109/ECCE47101.2021.9594967
View in ScopusGoogle Scholar

6. [6]

G. Ouyang, B. Jensen, C.R. Macziewski, T. Ma, F. Meng, Q. Lin, L. Zhou, M. Kramer, J. Cui
Characterization of ordering in Fe-6.5%Si alloy using X-ray, TEM, and magnetic TGA methods
Mater. Charact., 158 (2019), Article 109973, 10.1016/j.matchar.2019.109973
View PDFView articleView in ScopusGoogle Scholar

7. [7]

M.B. Richard
Iron silicon alloys
Ferromagnetism, IEEE (1978), pp. 67-101, 10.1109/9780470544624.ch4

Google Scholar
8. [8]
B. Wang, G. Li, Y. Wang, Y. Su, H. Sun, Z. Guo, D. Zhang, Z. Dong
Characterization of the Fe-6.5wt%Si strip with rapid cooling coupling deep supercooled solidification
ACS Omega, 6 (2021), pp. 25412-25420, 10.1021/acsomega.1c03367
View in ScopusGoogle Scholar
9. [9]
S. Cui, G. Ouyang, T. Ma, C.R. Macziewski, V.I. Levitas, L. Zhou, M.J. Kramer, J. Cui
Thermodynamic and kinetic analysis of the melt spinning process of Fe-6.5 wt.% Si alloy
J. Alloys. Compd., 771 (2019), pp. 643-648, 10.1016/j.jallcom.2018.08.293
View PDFView articleView in ScopusGoogle Scholar
10. [10]
C.D. Stanciu, T.F. Marinca, I. Chicinaş, O. Isnard
Characterisation of the Fe-10wt% Si nanocrystalline powder obtained by mechanical alloying and annealing
J. Magn. Magn. Mater., 441 (2017), pp. 455-464, 10.1016/j.jmmm.2017.06.010
View PDFView articleView in ScopusGoogle Scholar
11. [11]
M. Garibaldi, I. Ashcroft, N. Hillier, S.A.C. Harmon, R. Hague
Relationship between laser energy input, microstructures and magnetic properties of selective laser melted Fe-6.9%wt Si soft magnets
Mater. Charact., 143 (2018), pp. 144-151, 10.1016/j.matchar.2018.01.016
View PDFView articleView in ScopusGoogle Scholar
12. [12]
W.H. Teh, L.P. Tan, S. Chen, F. Wei, J.J. Lee, S.P. Padhy, V. Chaudhary, C.C. Tan, R.V. Ramanujan
Breaking conventional limits of silicon content in Fe-xSi magnetic alloys through additive manufacturing
J. Alloys. Compd., 983 (2024), Article 173829, 10.1016/j.jallcom.2024.173829
View PDFView articleView in ScopusGoogle Scholar
13. [13]
G. Stornelli, A. Faba, A. Di Schino, P. Folgarait, M.R. Ridolfi, E. Cardelli, R. Montanari
Properties of additively manufactured electric steel powder cores with increased Si content
Materials, 14 (2021), p. 1489, 10.3390/ma14061489
View in ScopusGoogle Scholar
14. [14]
W.F. Barrett
On the increase of electrical resistivity caused by alloying iron with various elements, and the specific heat of those elements
Proc. R. Soc. Lond., 69 (1902), pp. 480-485, 10.1098/rspl.1901.0135
Google Scholar
15. [15]
T.D. Zhou, P.H. Zhou, D.F. Liang, L.J. Deng
Structure and electromagnetic characteristics of flaky FeSiAl powders made by melt-quenching
J. Alloys. Compd., 484 (2009), pp. 545-549, 10.1016/j.jallcom.2009.04.145

View PDFView articleView in ScopusGoogle Scholar
16. [16]
K.-S. Lee, Y.-C. Yun, S.-W. Kim, S.-S. Kim
Microwave absorption of λ/4 wave absorbers using high permeability magnetic composites in quasimicrowave frequency band
J. Appl. Phys., 103 (2008), p. 07E504, 10.1063/1.2830827
View in ScopusGoogle Scholar
17. [17]
M. Han, D. Liang, J. Xie, L. Deng
Effect of attrition time on the microwave permeability of magnetic Fe-Si-Al flakes
J. Appl. Phys., 111 (2012), p. 07A317, 10.1063/1.3673813
View in ScopusGoogle Scholar
18. [18]
T. Ma, M. Yan, W. Wang
The evolution of microstructure and magnetic properties of Fe–Si–Al powders prepared through melt-spinning
Scr. Mater., 58 (2008), pp. 243-246, 10.1016/j.scriptamat.2007.10.017
View PDFView articleView in ScopusGoogle Scholar
19. [19]
L. Liu, Z.H. Yang, C.R. Deng, Z.W. Li, M.A. Abshinova, L.B. Kong
High frequency properties of composite membrane with in-plane aligned Sendust flake prepared by infiltration method
J. Magn. Magn. Mater., 324 (2012), pp. 1786-1790, 10.1016/j.jmmm.2011.12.038
View PDFView articleView in ScopusGoogle Scholar
20. [20]
F. Fiorillo, G. Bertotti, C. Appino, M. Pasquale
Soft magnetic materials
Wiley Encyclopedia of Electrical and Electronics Engineering (2016), pp. 1-42, 10.1002/047134608X.W4504.pub2
Google Scholar
21. [21]
V. Chaudhary, L.P. Tan, V.K. Sharma, R.V. Ramanujan
Accelerated study of magnetic Fe-Co-Ni alloys through compositionally graded spark plasma sintered samples
J. Alloys. Compd., 869 (2021), Article 159318, 10.1016/j.jallcom.2021.159318
View PDFView articleView in ScopusGoogle Scholar
22. [22]
L.P. Tan, V. Chaudhary, Z. Tsakadze, R.V. Ramanujan
Rapid multiple property determination from bulk materials libraries prepared from chemically synthesized powders
Sci. Rep., 12 (2022), p. 9504, 10.1038/s41598-022-13691-3
View in ScopusGoogle Scholar
23. [23]
R. Marder, C. Estournès, G. Chevallier, R. Chaim

Plasma in spark plasma sintering of ceramic particle compacts
Scr. Mater., 82 (2014), pp. 57-60, 10.1016/j.scriptamat.2014.03.023
View PDFView articleView in ScopusGoogle Scholar
24. [24]
M. Tokita
Trends in advanced SPS spark plasma sintering systems and technology, functionally gradient materials and unique synthetic processing methods from next generation of powder technology
J. Soc. Powder Technol., 30 (1993), pp. 790-804, 10.4164/sptj.30.11_790
Google Scholar
25. [25]
Z.-H. Zhang, Z.-F. Liu, J.-F. Lu, X.-B. Shen, F.-C. Wang, Y.-D. Wang
The sintering mechanism in spark plasma sintering – Proof of the occurrence of spark discharge
Scr. Mater., 81 (2014), pp. 56-59, 10.1016/j.scriptamat.2014.03.011
View PDFView articleGoogle Scholar
26. [26]
V. Chaudhary, N.M. Sai Kiran Kumar Yadav, S.A. Mantri, S. Dasari, A. Jagetia, R.V. Ramanujan, R. Banerjee
Additive manufacturing of functionally graded Co–Fe and Ni–Fe magnetic materials
J. Alloys. Compd., 823 (2020), Article 153817, 10.1016/j.jallcom.2020.153817
View PDFView articleView in ScopusGoogle Scholar
27. [27]
S.W. Fackler, V. Alexandrakis, D. König, A.G. Kusne, T. Gao, M.J. Kramer, D. Stasak, K. Lopez, B. Zayac, A. Mehta, A. Ludwig, I. Takeuchi
Combinatorial study of Fe-Co-V hard magnetic thin films
Sci. Technol. Adv. Mater., 18 (2017), pp. 231-238, 10.1080/14686996.2017.1287520
View in ScopusGoogle Scholar
28. [28]
M.L. Green, I. Takeuchi, J.R. Hattrick-Simpers
Applications of high throughput (combinatorial) methodologies to electronic, magnetic, optical, and energy-related materials
J. Appl. Phys., 113 (2013), Article 231101, 10.1063/1.4803530
View in ScopusGoogle Scholar
29. [29]
H. Xing, B. Zhao, Y. Wang, X. Zhang, Y. Ren, N. Yan, T. Gao, J. Li, L. Zhang, H. Wang
Rapid construction of Fe–Co–Ni composition-phase map by combinatorial materials chip approach
ACS Comb. Sci., 20 (2018), pp. 127-131, 10.1021/acscombsci.7b00171
View in ScopusGoogle Scholar
30. [30]
T. Borkar, R. Conteri, X. Chen, R.V. Ramanujan, R. Banerjee
Laser additive processing of functionally-graded Fe–Si–B–Cu–Nb soft magnetic materials
Mater. Manuf. Process., 32 (2017), pp. 1581-1587, 10.1080/10426914.2016.1244849
View in ScopusGoogle Scholar
31. [31]
S. Burger, C. Eberl, A. Siegel, A. Ludwig, O. Kraft

A novel high-throughput fatigue testing method for metallic thin films
Sci. Technol. Adv. Mater., 12 (2011), 10.1088/1468-6996/12/5/054202
054202-054202
Google Scholar

32. [32]
P. Decker, D. Naujoks, D. Langenkämper, C. Somsen, A. Ludwig
High-throughput structural and functional characterization of the thin film materials system Ni–Co–Al
ACS. Comb. Sci., 19 (2017), pp. 618-624, 10.1021/acscombsci.6b00176
View in ScopusGoogle Scholar

33. [33]
A. Ludwig
Discovery of new materials using combinatorial synthesis and high-throughput characterization of thin-film materials libraries combined with computational methods
NPJ. Comput. Mater., 5 (2019), p. 70, 10.1038/s41524-019-0205-0
View in ScopusGoogle Scholar

34. [34]
S.P. Padhy, Z. Tsakadze, V. Chaudhary, G.J. Lim, X. Tan, W.S. Lew, R.V. Ramanujan
Rapid multi-property assessment of compositionally modulated Fe-Co-Ni thin film material libraries
Res. Mater., 14 (2022), Article 100283, 10.1016/j.rinma.2022.100283
View PDFView articleView in ScopusGoogle Scholar

35. [35]
C. Li, H. Ruan, D. Chen, K. Li, D. Guo, B. Shao
Effect of heat treatment on the microstructure and properties of Ni based soft magnetic alloy
Microsc. Res. Tech., 81 (2018), pp. 796-802, 10.1002/jemt.23038
View in ScopusGoogle Scholar

36. [36]
V. Baheti, R. Abbasi, J. Militky
Ball milling of jute fibre wastes to prepare nanocellulose
World J. Eng., 9 (2012), pp. 45-50, 10.1260/1708-5284.9.1.45
Google Scholar

37. [37]
L.P. Tan, S.P. Padhy, Z. Tsakadze, V. Chaudhary, R.V. Ramanujan
Accelerated property evaluation of Ni–Co materials libraries produced by multiple processing techniques
J. Mater. Res. Technol., 20 (2022), pp. 4186-4196, 10.1016/j.jmrt.2022.08.152
View PDFView articleView in ScopusGoogle Scholar

38. [38]
J.S. Shin, J.S. Bae, H.J. Kim, H.M. Lee, T.D. Lee, E.J. Lavernia, Z.H. Lee
Ordering–disordering phenomena and micro-hardness characteristics of B2 phase in Fe–(5–6.5%)Si alloys
Mater. Sci. Eng. A, 407 (2005), pp. 282-290, 10.1016/j.msea.2005.07.012
View PDFView articleView in ScopusGoogle Scholar

39. [39]

P.R. Swann, L. Grånäs, B. Lehtinen
The B2 and DO3 ordering reactions in iron–silicon alloys in the vicinity of the curie temperature
Metal Sci., 9 (1975), pp. 90-96, 10.1179/030634575790445279
View in ScopusGoogle Scholar
40. [40]
M. Amoohadi, M. Mozaffari, A. Gharaati, M. Rezazadeh
Structural and magnetic properties of ordered/disordered sendust powders prepared by mechanical alloying
J. Supercond. Nov. Magn., 31 (2018), pp. 2547-2552, 10.1007/s10948-017-4473-y
View in ScopusGoogle Scholar
41. [41]
X. Peng, A. Zhang, J. Li, S. Yu, J. Chang, M. Ge, Y. Yang, J. Xu, B. Hong, D. Jin, H. Jin, X. Wang, H. Ge, J. Fang
Design and fabrication of Fe–Si–Al soft magnetic composites by controlling orientation of particles in a magnetic field: anisotropy of structures, electrical and magnetic properties
J. Mater. Sci., 54 (2019), pp. 8719-8726, 10.1007/s10853-019-03470-3
View in ScopusGoogle Scholar
42. [42]
Z. Luo, X.a. Fan, W. Hu, F. Luo, J. Wang, Z. Wu, X. Liu, G. Li, Y. Li
Properties of Fe_2SiO_4/SiO_2 coated Fe-Si soft magnetic composites prepared by sintering Fe-6.5wt%Si/Fe_3O_4 composite particles
J. Magn. Magn. Mater., 499 (2020), Article 166278, 10.1016/j.jmmm.2019.166278
View PDFView articleView in ScopusGoogle Scholar
43. [43]
Q. Li, Z. Feng, S. Yan, Y. Nie, X. Wang
Comparison of the magnetic and absorption properties of flaky super sendust and sendust alloys
J. Electron. Mater., 44 (2015), pp. 3777-3782, 10.1007/s11664-015-3847-9
View in ScopusGoogle Scholar
44. [44]
E. Legarra, E. Apiñaniz, F. Plazaola
Influence of the order-disorder transition on the magnetic properties of $Fe_{75}Al_{25-x}Si_x$ alloys
Intermetallics, 69 (2016), pp. 35-41, 10.1016/j.intermet.2015.10.008
View PDFView articleView in ScopusGoogle Scholar
45. [45]
R.D. Cava, W.J. Botta, C.S. Kiminami, M. Olzon-Dionysio, S.D. Souza, A.M. Jorge, C. Bolfarini
Ordered phases and texture in spray-formed Fe–5wt%Si
J. Alloys Compd., 509 (2011), pp. S260-S264, 10.1016/j.jallcom.2010.11.184
View PDFView articleView in ScopusGoogle Scholar
46. [46]
J. Wang, X. Liu, C. Lei, X. Mao, D. Liu, X.a. Fan, Z. Luo, F. Luo
Core loss reduction for Fe-6.5wt%Si soft magnetic composites doped with Co element
J. Magn. Magn. Mater., 502 (2020), Article 166553, 10.1016/j.jmmm.2020.166553
View PDFView articleView in ScopusGoogle Scholar
47. [47]

T. Kang, S. Wu, M. Wang, J. Wang, X. Fan, Y. Lu
Novel Fe2CoNi(AlSi)x high-entropy alloys with attractive soft magnetic and mechanical properties
Appl. Phys. A., 127 (2021), p. 829, 10.1007/s00339-021-04988-7
View in ScopusGoogle Scholar
48. [48]
J. Ding, Y. Li, L.F. Chen, C.R. Deng, Y. Shi, Y.S. Chow, T.B. Gang
Microstructure and soft magnetic properties of nanocrystalline Fe–Si powders
J. Alloys. Compd., 314 (2001), pp. 262-267, 10.1016/S0925-8388(00)01234-2
View PDFView articleView in ScopusGoogle Scholar
49. [49]
V. Chaudhary, R.V. Ramanujan
Magnetocaloric properties of Fe-Ni-Cr nanoparticles for active cooling
Sci. Rep., 6 (2016), p. 35156, 10.1038/srep35156
View in ScopusGoogle Scholar
50. [50]
A. Arzhnikov, L. Dobysheva, E. Elsukov, A. Zagainov
Concentration dependence of the magnetization and the Curie temperature in disordered Fe-M alloys (M= Al, Si, Sn)
J. Exp. Theoret. Phys., 83 (1996), pp. 623-627
Google Scholar
51. [51]
G.V. Samsonov
Electrical and magnetic properties of the elements
G.V. Samsonov (Ed.), Handbook of the Physicochemical Properties of the Elements, Springer US, Boston, MA (1968), pp. 314-373, 10.1007/978-1-4684-6066-7_5
Google Scholar
52. [52]
G.V. Samsonov
Mechanical properties of the elements
G.V. Samsonov (Ed.), Handbook of the Physicochemical Properties of the Elements, Springer US, Boston, MA (1968), pp. 387-446, 10.1007/978-1-4684-6066-7_7
Google Scholar
53. [53]
A. Boulouma, A. Gangopadhyay, A. Ain-Souya, A. Drici, A. Amara
Effect of Si on the magnetic and mechanical properties of arc melted soft magnetic Fe-Si-Al alloys
Indian J. Sci. Technol., 10 (21) (2017), 10.17485/ijst/2017/v10i21/111492
Google Scholar
54. [54]
G. Ouyang, B. Jensen, W. Tang, K. Dennis, C. Macziewski, S. Thimmaiah, Y. Liang, J. Cui
Effect of wheel speed on magnetic and mechanical properties of melt spun Fe-6.5 wt.% Si high silicon steel
AIP Adv., 8 (2018), Article 056111, 10.1063/1.5006481
View in ScopusGoogle Scholar
55. [55]

H. Yu, Y. Wen, X. Bi
Magnetic and mechanical properties of the gradient FeSi alloys fabricated by magnetron sputtering
J. Alloys Compd., 634 (2015), pp. 83-86, 10.1016/j.jallcom.2015.01.156
View PDFView articleView in ScopusGoogle Scholar

56. [56]

T.E. Buchheit, J.D. Carroll, B.G. Clark, B.L. Boyce
Evaluating deformation-induced grain orientation change in a polycrystal during in situ tensile deformation using EBSD
Microsc. Microanal., 21 (2015), pp. 969-984, 10.1017/s1431927615000677
View at publisherView in ScopusGoogle Scholar

57. [57]

P. Jang
Effects of annealing on structure and magnetic properties of Fe-Si-Al flakes
Korean J. Met. Mater., 56 (2018), pp. 680-685, 10.3365/KJMM.2018.56.9.680
View at publisherView in ScopusGoogle Scholar